scientific reports

Geometrical constraint change determines organized collective migration of follower cells

Mitsuru Sentoku[1], Masaharu Endo[1], Miki Takei[1], Wataru Hanamoto[2] & Kenji Yasuda[1,2]✉

Spatial confinement plays a critical role in shaping collective cell migration, particularly in regulating interactions between leader and follower cells and among follower cells themselves. However, how changes in confinement geometry influence migration dynamics and cell-to-cell interactions remains poorly understood. This study leverages a novel microchannel design to systematically dissect the interplay between spatial confinement and collective cell behavior in endothelial-like cells (MILE SVEN 1). In a single-cell-wide T-shaped branching structure, rear cells selected alternate pathways, avoiding direct alignment with preceding cells. This highlights how spatial geometry mediates follower-follower interactions by encouraging dynamic rearrangements within the cell train. Ladder-like branching structures with consistent total pathway widths showed that dividing and reassembling cell trains had minimal impact on migration velocity, provided no compression or expansion occurred. Wide-narrow-wide patterns demonstrated distinct effects: stepwise transitions accelerated cells in narrow sections, increasing directional alignment driven by spatial restriction, followed by decreased alignment in wider regions. Gradual transitions maintained stable alignment and minimized disruptions, emphasizing the importance of smooth geometrical transitions in preserving robust collective behavior. These findings reveal how spatial confinement integrates follower-follower interactions and dynamic realignment. By linking geometric transitions to collective cell dynamics, our study advances the understanding of physical guidance mechanisms and offers a platform for investigating spatial influences on migrating cellular systems.

Collective cell migration underpins many biological processes, from maintaining tissue integrity to responding to physiological demands[1–3]. This migration is driven by collective polarization, where cells align their directional signals to achieve cohesive movement. Mechanochemical coupling and dynamic cytoskeletal rearrangements facilitate this alignment, enabling motility and inducing shape changes[4–8]. In vascular development, endothelial cells migrate collectively to form blood vessels, enabling tissue growth and repair during processes like angiogenesis and wound healing[9–12]. However, this migration also contributes to pathological events, such as tumor angiogenesis and the formation of leaky vessels in inflammatory diseases, underscoring its dual roles in health and disease[13,14]. While coordination between the front and rear of cell monolayers is vital for these events[15,16], the mechanisms regulating collective migration, particularly in response to spatial and geometric constraints, remain poorly understood. Addressing these gaps is crucial for deciphering how endothelial cells adapt their collective behavior across physiological and pathological contexts.

Front cells at the leading edge of the monolayer, exhibiting dominant lamellipodial protrusions driven by the interplay between Rac and RhoA GTPases[17–21], are recognized as leader cells. These cells play a pivotal role in collective migration by sensing and responding to external cues, such as during sprouting angiogenesis, where tip cells guide stalk cells along vascular networks[22]. When a cell group migrates through a complex microenvironment, the change of the position of front cells and rear cells can exchange the role of leader cells and followers during migration *in vitro* as well as *in vivo*[9,23,24]. For example, tip cells in the tracheal branches of *D. melanogaster*remain stable during the entire morphogenesis process[25], while the leaders of border cells frequently change[26,27]. Studies have shown that local mechanical forces play a crucial role in the emergence of leader cells, acting to inhibit neighboring cells from adopting a leader-like fate even before leader cells fully differentiate[28]. Additionally, recent work utilizing optogenetics to induce leader-like phenotypes has estimated that leader cells influence only their immediate neighbors, with an effective range limited to a single follower cell. This finding underscores the importance of localized mechanical and signaling interactions in coordinating collective migration[29]. Rear cells play a complementary follower role by maintaining group cohesion and transmitting

[1]Department of Pure and Applied Physics, Graduate School of Advanced Science and Engineering, Waseda University, Tokyo 169-8555, Japan. [2]Department of Physics, School of Advanced Science and Engineering, Waseda University, Tokyo 169-8555, Japan. ✉email: yasuda@list.waseda.jp

mechanical forces across the migrating population through their interactions with both leader cells and adjacent followers[6]. However, how these mechanisms integrate under spatial constraints to drive coordinated migration remains poorly understood.

The collective behavior of migrating cells is influenced not only by biochemical signals, such as VEGF, during angiogenesis but also by the spatial geometry of their microenvironment. Previous studies have shown that confinement and geometrical characteristics can significantly affect migration behavior by adjusting the cell-cell interaction[30,31]. For instance, in microfluidic devices, narrow channels have been shown to promote faster migration speeds and increased alignment, while wider spaces often result in less cohesive movement due to greater degrees of freedom[32,33]. These *in vitro* studies covering the relation between confinement width and cellular dynamics have been corroborated *in vivo*zebrafish and Xenopus embryos for neural crest cells, where the migration efficiency of specific cell cluster sizes are enhanced by optimal confinement widths[34]. Similarly, patterned substrates induce morphological changes in cells, which entail cytoskeletal reorganization that regulates the protrusive ability of the cells[35]. However, while these studies provide a foundation for understanding collective migration in controlled environments, they often focus on leader cells or overall population behaviors without dissecting how spatial geometry modulates cell-to-cell interactions, particularly among follower cells. A recent study employed micropatterned substrate to examine these interactions at a single-cell level, emphasizing the contact inhibition of locomotion (CIL) and contact following locomotion (CFL) behavior of epithelial cells, suggesting that the intercellular behavior was different based on the location of the contact site[36]. The interplay between physical confinement and mechanisms such as CIL and CFL requires further investigation to understand how these individual mechanical interactions contribute to the emergent properties of coordinated dynamics in cell collectives.

While prior research has provided valuable insights into the collective migration of cells, several limitations remain. Many studies have predominantly focused on leader cells, emphasizing their roles in sensing external cues and initiating directional migration, often underestimating the contributions of follower cells that possess leadership potential[15,24]. Additionally, while biochemical signaling pathways, such as those driven by VEGF, have been extensively studied, the physical and mechanical interactions between cells under varying spatial constraints are less understood. Previous investigations into geometrical confinement have largely concentrated on static behaviors, such as migration speeds and alignment in fixed-width channels, without considering how dynamic spatial transitions, such as compression and expansion, influence collective behaviors[33,35]. Furthermore, the majority of studies addressing CIL and CFL mechanisms have done so in the context of uniform, unconfined environments, leaving the interplay of these processes under spatially varying constraints largely unexplored. These limitations underscore the need for a more comprehensive approach that integrates spatial geometry, physical interactions, and CIL/CFL dynamics, particularly in the context of follower cells, to understand the adaptive mechanisms underlying collective migration fully.

In this study, we aim to address these limitations by systematically investigating the interplay between spatial geometry, cell-to-cell interactions, and migration mechanisms in two-dimensional (2D) confined environments, with additional insights gained from a three-dimensional (3D) experiment to bridge the findings to physiological contexts. Using a series of microfabricated patterns, we explore how geometrical confinement and dynamic spatial transitions influence collective behaviors, focusing on the less-studied roles of follower cells and the balance between CIL and CFL. By examining T-shaped branching, stepwise and gradual wide-narrow-wide patterns, and inverted bicone microtunnels, we seek to uncover the dominant factors regulating collective migration under varying spatial constraints. These findings aim to advance our understanding of how physical environments regulate collective behaviors, providing a foundation for exploring their relevance in complex biological systems.

Results

Stepwise agarose microstructure formation for collective cell migration measurement

In this experiment, we used agarose microfabrication technology to examine the role of confinement structures in collective migration behaviors. The advantages of agarose microstructures over conventional microstructures like SU-8 and microprinting patterns are the freedom of pathway height with no rid and adhesion factors and flexible change of pathway patterns even during cultivation. In this technology, when the shapes of cell reservoirs and micropathways are fabricated in the thin agarose layer covered on the bottom surface of the culture dish, cells attach and migrate in the fabricated agarose-free region only because they cannot attach and climb up to the agarose layer region. Exploiting these advantages of agarose microstructures, we have observed collective cell migration behavior in the agarose-based micropatterns.

The schematic of the collective cell migration measurement assay set in the 1064/1480-nm laser photo-thermal microfabrication system is described in Fig. 1 **A**. Cell reservoir chamber and micropathways were stepwisely fabricated in a thin agarose layer coated on the culture dish, exploiting the microfabrication process illustrated schematically in Fig. 1 **B**. The shutter controller regulates the emission of the focused 1480-nm wavelength infrared (IR) laser, which is irradiated via the objective lens (x20 obj. PLAN Apo, Olympus, Tokyo, Japan). When the laser is irradiated onto the agarose-coated culture dish containing water (or DMEM medium), the water absorbs the focused laser and emits heat. Consequently, a portion of the agarose layer at the focused laser spot area melts, enabling μm resolution microfabrication of agarose-free patterns of interest. Finally, the vascular endothelial cells attach only to the exposed agarose-free region of the tissue culture dish for proliferation.

Figures 1 **B** and **C** represent the schematic illustrations and micrograph images of the stepwise reservoir and microchannel formation for collective cell migration observation. First, we fabricated the 0.5×2 mm reservoir chamber on the agarose layer of the dish (Figs. 1**B (a)** and **C (a)**). Then, 3×10^4 MS-1 cells were seeded on the cultivation dish, and only the cells in the reservoir chamber adhered (Figs. 1**B (b)** and **C (b)**). After the MS-1 cells proliferated and became confluent, microchannels were added to the reservoir chamber (Figs. 1**B (c)** and

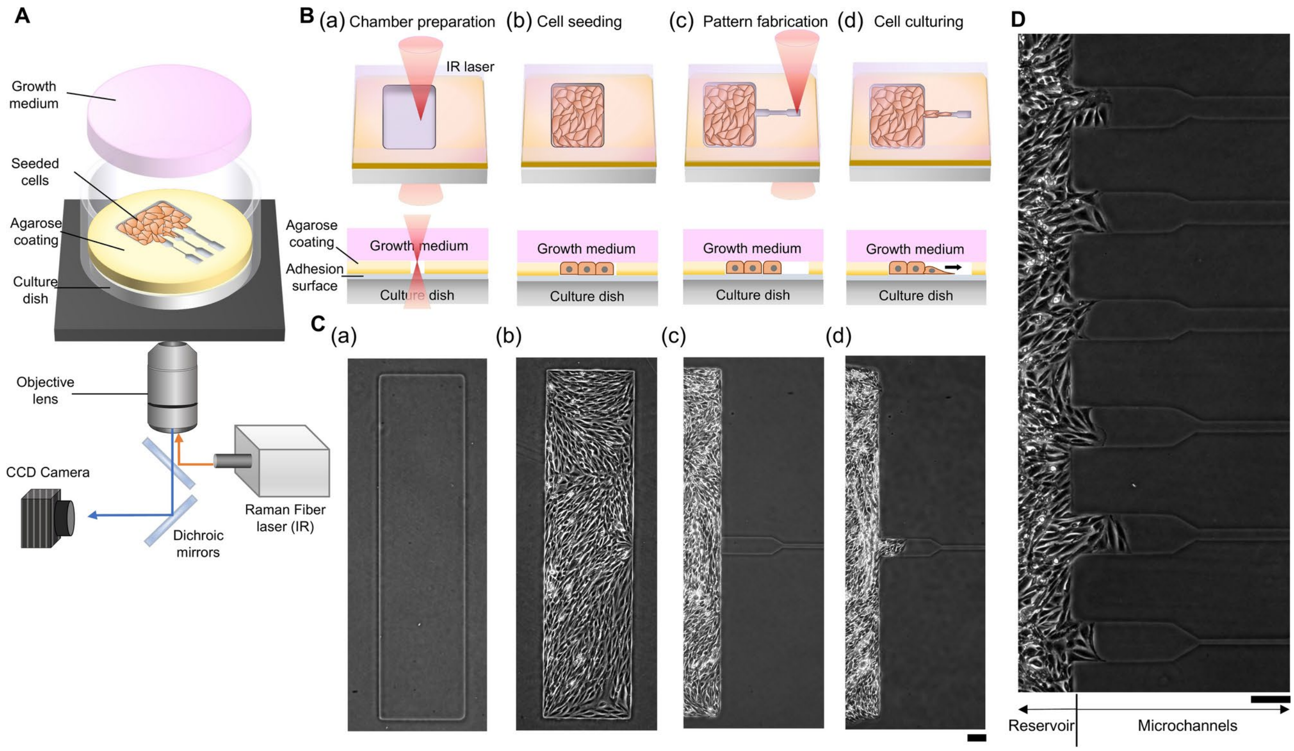

Fig. 1. Microfabricated agarose structures to confine and regulate the spatio-temporal migration of endothelial cell line, MILE SVEN 1 (MS-1). (**A**) Illustration of the layers inside the culture dish and the employment of laser irradiation for microfabrication. Briefly, a thin agarose layer is coated on the adhesion bottom surface of the cultivation dish. Agarose microstructures were formed by the spot heating of a focused infrared (IR) laser from the 1064/1480-nm laser photo-thermal microfabrication system. (**B**) Schematic illustration of the stepwise agarose micropattern formation process and culturing endothelial cells: Upper, overhead views; lower, side cross-sectional views). (**a**) The confinement cultivation chamber is first produced using the heat from focused infrared laser absorption. (**b**) The cells were seeded and cultivated until ample cells covered the chamber area. (**c**) Additional microfabrication was conducted to create the desired micropattern to induce cell migration. (**d**) Observation of the cells migrating inside the fabricated channel. (**C**) Phase contrast images of MS-1 cells in agarose microstructures respective to the illustration of the pattern formation procedures in (**B**). (**D**) Micrograph image of cells starting their progression into all microchannels after connecting to the reservoir simultaneously. Bars 100µm.

C (c)). Finally, the cell migration from the cell reservoir into the channels was culturing dish was observed with timelapse capturing in collective cell migration measurement assay (Figs. 1**B** (**d**) and **C** (**d**)).

As demonstrated in Fig. 1 **C**, MS-1 cells were successfully captured and cultivated in the agarose-free region within the walls of agarose-etched patterns of the reservoir and microchannels, and no cells climbed over these walls. With this two-step microfabrication, we also observed the smooth migration of MS-1 cells from the confluent cell reservoir to a newly added microchannel (Fig. 1 **C**(d)). Moreover, no signs of cell apoptosis were observed during the microfabrication process, provided that the laser did not directly irradiate the cells and the power was controlled. Furthermore, a similar microfabrication method was employed in our previous studies, where no apparent damage to this cell type was reported[32]. Thus, we concluded that this photo-thermal etching technique is harmless to cells, allowing additional etching even after cells are seeded.

Figure 1 **D** shows the micrograph image of cell movements from the reservoir to six microchannels after opening those microchannels simultaneously connected to the reservoir (15 hours). As shown in this picture, the cells began to advance into the microchannels similarly at this early stage. This ability to align the start time of cell migration into multiple microchannels was used in our experiments to compare differences in collective cell migration rates between them.

T-shape division experiment of single-cell train for cell-to-cell interaction measurement

For follower cells in collective migration, two primary types of cell-to-cell interactions are considered: front-to-rear and neighboring rear-to-rear interactions. To explore these dynamics, we first evaluated the interactions between neighboring rear cells and the influence of front cells on rear cells within a single-cell train. Specifically, we analyzed the pathway selection of individual cells in a single-cell-wide T-shaped micropattern, determining whether cells followed the same branch as the preceding cell or selected the alternative branch. In the absence of interactions between cells, the distribution of rear cells across the two branches should follow a Bernoulli trial model, where an equal probability exists for selecting either branch (see Fig. S1). Deviations from this expected distribution would indicate the presence of attractive or repulsive forces, either mechanical or biochemical, between the cells.

Figure 2 presents the results of the number distribution of single cells, progressing in series through a T-shaped bifurcation, either following the front cell into the same branch ('Branch I') or entering the opposite branch ('Branch II'). Figure 2 **A** shows a schematic representation, while Figure 2 **B** contains optical micrographs

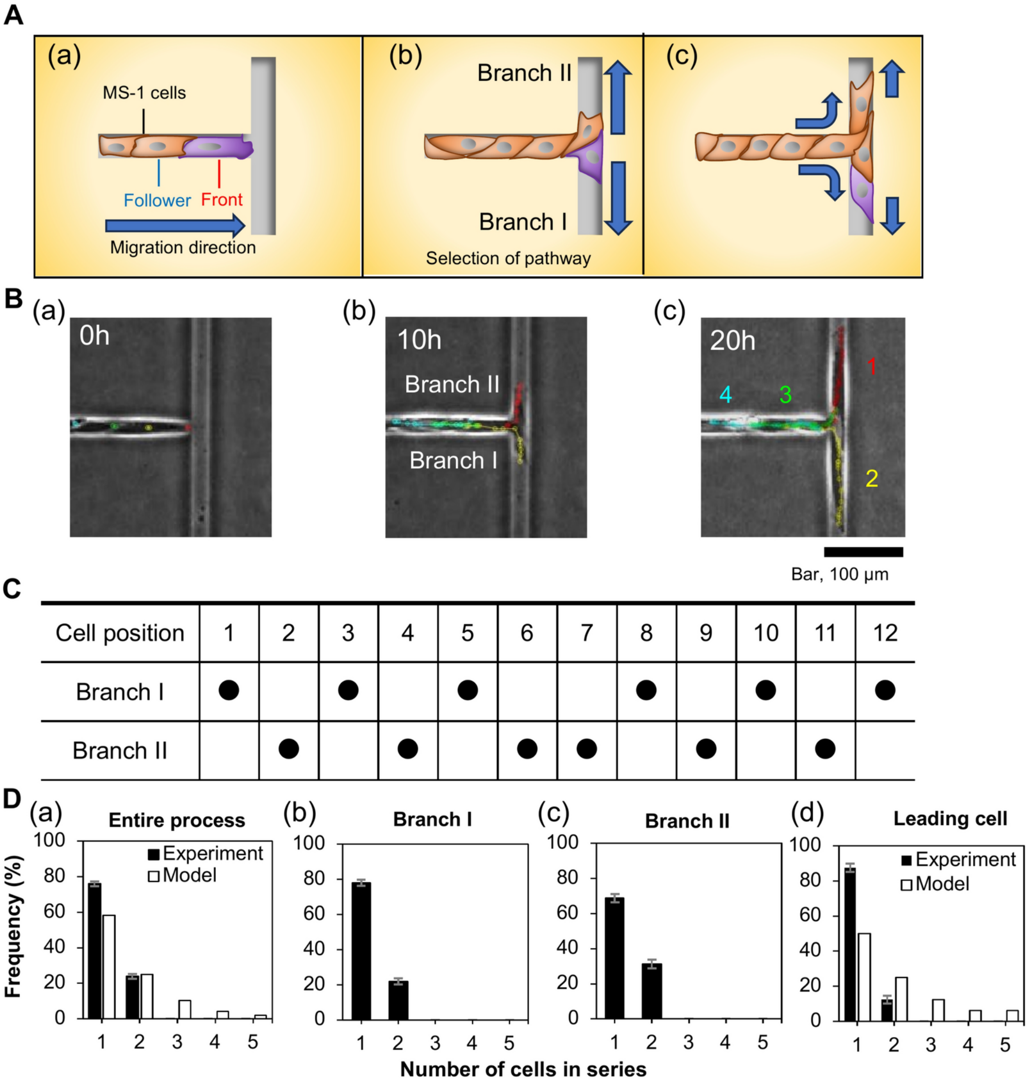

Cell position	1	2	3	4	5	6	7	8	9	10	11	12
Branch I	●		●		●			●		●		●
Branch II		●		●		●	●		●		●	

Fig. 2. Measurement of cell-to-cell interactions in single-cell train using a T-shaped bifurcated microchannel. (**A**) and (**B**) Schematic diagrams and micrographs showing the selection process in which the rear cells choose the same or opposite destination as the leading front cell at the bifurcation point of a T-shaped microchannel. When the leading front cell enters the downward-branching channel, we call this "Branch I," and the other upward-branching channel "Branch II." The time when the leading front cells reach the junction (**a**) is set as 0 h, and the following diversion processes of follower cells represented here are for (**b**) 10 h and (**c**) 20 h after the cells reach the junction. In Fig. (**A**), the front cell is represented by purple color while the remaining following cells are represented as orange. (**C**) A representative table exhibiting the order in which the cells entered the branches for MS-1 cells. Filled circles in the table indicate which branch the rear cell selected (position 2–12) after the leading front cell (position 1) entered Branch I. From these measured cell order, the first five cells of each replicate were used for the following analysis. (**D**) A graphical comparison of the number of cells that entered each branch in series for MS-1. **(a)** The consecutive number distribution of cells when the front and four rear cells moved into the T-shape branch. **(b)** The consecutive number distribution of cells entering Branch I in the distribution (**a**). **(c)** The consecutive number distribution of cells entering Branch II in the distribution (**a**). **(d)** The consecutive number distribution of cells that followed the front cell entering Branch I in the distribution (**a**). The "experiment" (filled bars) represents the obtained number distribution of the cell streaks during the branch selection behavior of the first five cells from 16 experimental samples (N=16). The "model" (open bars) is calculated using the Bernoulli trial for independent lined five particles neglecting particular interactions (see Fig. S1). The error bars represent the standard deviation determined using bootstrapping.

of MS-1 cell migration within the T-shaped branching microchannel. Cells traveled along a single-cell-wide pathway from the reservoir as a single-cell train, reaching the T-shaped bifurcation (**a**), where the rear cells made their two-way branch selections (**b**). To illustrate the sequence of branch selection, Figure 2 **C** records the cell position and the pathway choice for each cell. 'Cell position' refers to the order in which the cells follow the front cell, with position '1' indicating the front cell, position '2' indicating the next cell, and so on. The filled circles represent the selected branch for each cell. For instance, the front cell (position 1) moved into Branch I, while the second cell (position 2) chose Branch II. The subsequent cells alternated between Branch I and Branch II, forming a fragmented migration pattern. We repeated this experiment with 16 independent samples (N=16), generating a similar table for each experiment.

The consecutive number distribution of cells is summarized in Figure 2 **D**. In these distribution graphs, we recorded the number of consecutive cells selecting the same branch for the first five cells behind the front cell across 16 independent samples (indicated by filled bars). We focused on the first cells in each train to minimize the influence of downstream environmental factors.

As shown in Fig. 2 **D** (**a**), more than 76% of the cells selected different branches from their predecessors, suggesting that interactions between front and follower cells were minimal. A theoretical Bernoulli model (open bars in Fig. 2 **D** and Sup. Fig. 1), which assumes no interactions, predicted equal branch selection probabilities, but our results showed a significantly higher occurrence of isolated single cells, implying a repulsive mechanism at play. Notably, two-cell streaks were observed in only 24% of cases, with no streaks larger than two cells, whereas the model predicted that 17% of cells would form streaks larger than two. The model assumed an equal probability for single cells in Branch I and Branch II, yet our experimental results showed a significantly higher occurrence of isolated single cells compared to the theoretical model.

To further investigate the branch selection behavior, we replotted the consecutive number distributions for Branch I and Branch II (Figs. 2 **D** (**b**) and (**c**)). The distribution for single cells in Branch I was 78%, and in Branch II, 69%, while for two-cell clusters, it was 22% and 31%, respectively. Despite the front cells moving into Branch I, the distributions for Branch I and Branch II were similar, and the population of two-cell clusters in Branch I was lower than expected based on front-rear cell interactions. These findings suggest that there is no apparent attraction between neighboring cells, including front-follower cells, in single-cell trains under these conditions. Instead, the data indicate a repulsive tendency in this T-shape branching experiment.

We then focused specifically on the interaction between the front and second cells. Reanalysis of the same sample set (N=16) (Fig. 2 **D** (**d**) revealed that around 92% of second cells deviated from the front cell's trajectory, selecting the opposite branch. Only 12% of the second cells followed the front cell into the same branch, and no additional cells joined this pair. Thus, the maximum number of connected cells in proximity to the front cell was limited to two, much lower than the overall distribution seen in Fig. 2 **D** (**a**).

According to a probabilistic model based on the Bernoulli trial for a five-cell selection scenario, the predicted distribution suggests that 50% of cases should involve isolated front cells, 25% should form two-cell clusters, and the remaining 25% should involve clusters of three or more cells (Sup. Fig. 1). However, in our experimental setup, only single- and two-cell clusters were observed, with no occurrences of clusters containing three or more cells. Furthermore, we noted a slight increase in the proportion of single-cell cases and a reduction in two-cell clusters compared to the overall consecutive cell number distribution of the entire process presented in Fig.2 **D** (**a**).

Branching dependence of propagation manners in ladder-like division and reassembly confinement structure under conservation of total widths

Following examining front-to-rear and rear-to-rear cell interactions in the T-shaped branching structures, we extended our analysis to understand how the collective behavior of cell trains changes when divided and reassembled using different confinement geometries. To explore this, we designed three types of branching and reassembly patterns to study how migrating cells behave when confined to single-cell-wide or wider pathways, both during and after division into isolated cell trains.

As shown in Fig. 3, we have prepared three types of branching and reassembly patterns: a ladder-like single-cell-wide (25μm) three-branch division pathway (**A**)(N=8), a single-cell-wide four-branch division pathway (**B**)(N=7), and a combination of single-cell-wide and three-cell-wide (75μm) two-branch division pathways (**C**)(N=6). In all cases, the widths of the pathways before division and after reassembly were kept equal to the total summed width of the divided pathways to prevent compression or expansion effects (Figs. 3 (**a**) and (**b**)). This allowed us to isolate the effects of cell division and reassembly on collective migration without introducing confounding effects from changes in pathway width.

In the division process for pathways in Figs.3 **A** and **B**, front cells at the leading edge of the migrating cell sheet were separated into single cells as they entered the narrow, single-cell-wide branches. The interactions between these front cells and their rear followers became restricted to one-dimensional interactions. We observed the movement of these isolated single-cell trains within the narrow pathways, allowing us to evaluate their propagation speed and interactions without the influence of neighboring cells (Figs. 3 **A** and **B**). In the different width branching pattern (Fig. 3 **C**), where cells entered both single-cell-wide (left) and three-cell-wide (right) branches, we observed more complex interactions. The simultaneous comparison between single-cell-wide and three-cell-wide branches allowed us to evaluate the influence of neighboring cells in wider pathways.

It should be noted that both the front and rear cells were equally divided into branches without any localization or clustering during their forming of single-cell trains. This homogeneous spreading and division of cells might be caused by the similar repulsive/attractive interactions of cells observed in the T-shape branching in Fig. 2(**b**).

Next, we examined the migration velocity of the cell trains after division and reassembly. Despite the differences in pathway width and confinement, the average migration velocities across all channels and branching patterns remained consistent. Whether the cells were in single-cell-wide or three-cell-wide pathways, their mean

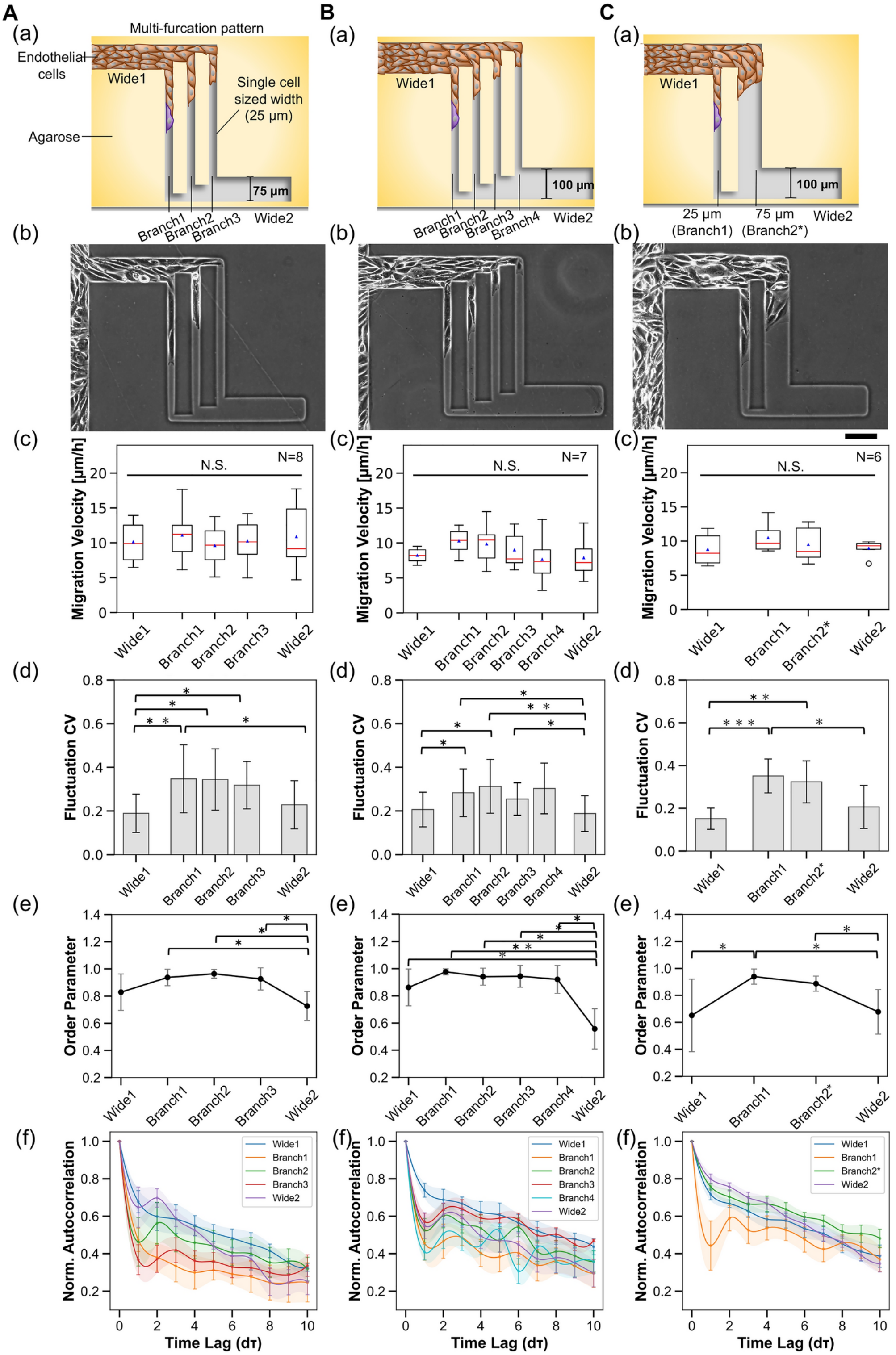

propagation velocity did not significantly change, as long as the total width of the micropattern was conserved (Figs. 3 (**c**)). Further comparisons between each channel were accomplished using an analysis of variance followed by a pairwise t-test, indicating that no significant differences were observed within the distributions.

On the other hand, the fluctuation observed in the collective cell dynamics indicated a significant difference between the main channel (before separation, Wide1) and the branches, as shown in Figs. 3 (**d**). The coefficient of variation (CV) was calculated as the ratio of the standard deviation to the mean, providing a normalized measure of fluctuation in migration velocity. This increase in fluctuations occurred in both single-cell-wide and three-cell-wide pathways. The branches demonstrated a more significant fluctuation in collective migration velocity than the main channels (Wide1). Upon reassembly in the Wide2 channel, the migration velocity fluctuations, which had increased during the confined branching phase, were reduced, indicating a partial

◀**Fig. 3**. Migration profile of collective endothelial cells inside branching and reassembling patterns to assess the influence of individual (front and neighboring) cells on the migrating cohort. (**A**) The collective cell migration profile of the MS-1 cells inside 3 branching patterns (N=8). The cell invasion through the main (first) channel into the 3 branches having a $25\mu\mathrm{m}$ single-cell-sized width (Branch1, Branch2, Branch3), followed by reassembly of the branches. (**B**) The collective cell migration profile inside the 4 branching $25\mu\mathrm{m}$ single-cell-sized width patterns (Branch1, Branch2, Branch3, Branch4), followed by reassembly of the branches (N=7). (**C**) The collective cell migration profile inside the different width branches (single-cell-sized width ($25\mu\mathrm{m}$) and three-cell-sized width ($75\mu\mathrm{m}$), followed by reassembly of the branches (N=6). (**a**) Illustrations of three patterns (**A**), (**B**), and (**C**). (**b**) The phase contrast images of the cells confined inside a microfabricated agarose pattern. The narrow branches are all $25\mu\mathrm{m}$ (see Fig. S2 for velocity vector tracks of those migrating cells). (**c**) The migration velocity of the cell sheet inside each channel: Before division (Wide1), branches ($25\mu\mathrm{m}$, Branch1, Branch2, Branch3, and Branch4; $75\mu\mathrm{m}$, Branch2*), after reassembly (Wide2) where the widths were based on the number of branches to maintain the total pathway width throughout the pattern. (**d**) The fluctuation given by the coefficient of variation (CV) graph demonstrates the fluctuation of the migration velocity of the cell sheet observed inside the channels. (**e**) Order parameters of the cell migration velocity vectors at different locations of the patterns. (f) The autocorrelation analysis of collective cell migration before branching (pre-separation), during branching (Branches), and after reassembling. The error bars represent the standard error of the mean across the ensemble of measured channels. *P < 0.05, **P < 0.01, ***P < 0.001. Bar, $100\mu\mathrm{m}$.

recovery of collective stability. These results indicate that independent of the branching width, the splitting process increases the fluctuations in migration velocity while the reassembling process decreases them.

To further assess the effects of division and reassembly on the organization of cell movement, we measured the order parameter, which evaluates the alignment of cells in the direction of migration (Fig. 3 (**e**)). As shown in previous reports, order parameters have been used to evaluate the directionality of migrating cells as a useful descriptor[20,33,37]. Using the same method as in previous reports, we analyzed the order parameter of the moving velocity vector of migrating cells, $S^{pol} = \langle \cos\theta \rangle$, where θ is the angle between the direction of local cell movement velocities and that of micropathway direction. The order parameter increased slightly as the cells migrated through the single-cell-wide pathways, suggesting that cells maintain some degree of directional alignment even in confined spaces. However, after reassembly into the wider pathways, the order parameter decreased, indicating that the division into single-cell-wide branches disrupted the collective alignment of the cells. In contrast, cells that reassembled in the wider three-cell-wide pathways maintained their pre-separation order parameter, suggesting that the presence of side-by-side interactions in wider pathways helps preserve coordinated movement.

Finally, we analyzed the velocity autocorrelation function, which quantifies the degree to which cell velocities at different points in time are correlated (Fig. 3 (**f**)). The velocity autocorrelation function $C(dt) = \langle \vec{v}(t) \cdot \vec{v}(t+dt) \rangle / \langle \vec{v}(t)^2 \rangle$, where $\vec{v}(t)$ is the velocity of the cells at time *t*, $\langle \cdots \rangle$ denotes average over time *t*. A high autocorrelation indicates that cells tend to maintain similar velocities over time, while a low autocorrelation suggests that cell velocities fluctuate more unpredictably. In this study, velocity autocorrelation was computed separately within each channel, ensuring that the measurement reflects local migration dynamics rather than influences from the end boundaries of the micropattern. This method captures the persistence of movement within confined regions, allowing us to assess how spatial confinement affects velocity coordination among cells. The autocorrelation decreased significantly when the cells entered the single-cell-wide pathways in all scenarios, reflecting a disruption in the coherence of their movement. In most cases, this reduction persisted even after reassembly, indicating that the division into single-cell-trains impaired their collective coordination (Fig.3 **A**(**f**) and **B**(**f**)). However, in the case of cells that reassemble from the single-cell train ($25\mu\mathrm{m}$) pathway and the wider ($75\mu\mathrm{m}$) three-cell-wide pathway, the autocorrelation recovered, suggesting that wider pathways allow for the restoration of more consistent and coordinated movement (Fig.3 **C**(**f**)).

Width dependence of propagation manners in stepwise wide-narrow-wide confinement structures

As shown in Fig. 3, we observed that the collective migration velocity remained largely unchanged after passing through the branching and reassembly micropatterns, as long as the total confinement width was preserved. This indicates that the average migration velocity is maintained as long as there are no significant changes in the confinement width that would compress or allow the cells to expand. However, given previous studies reporting that channel width can influence migration dynamics-typically showing faster migration in narrower channels[32,33,38]-we sought to explore how cell dynamics, particularly migration velocity and order, could be altered by regulating local cell-cell interactions via changes in confinement width.

To achieve this, we designed a stepwise wide-narrow-wide confinement structure to test how cell-cell interactions shift during compression and expansion. Collective cell migration was observed inside straight channels with an initial width of $100\mu\mathrm{m}$, followed by a narrow section with varying widths of $20\mu\mathrm{m}$, $30\mu\mathrm{m}$, and $50\mu\mathrm{m}$, before expanding back to the original width of $100\mu\mathrm{m}$ sequentially (wide-narrow-wide confinement) (Fig. 4 **A** and **B**). The narrow widths were chosen to be (a) $20\mu\mathrm{m}$, (b) $30\mu\mathrm{m}$, and (c) $50\mu\mathrm{m}$ as previously we have demonstrated that there's a maximum migration velocity around $30\mu\mathrm{m}$and when the channel width is narrower or wider, the overall cell dynamics decreases in the straight channels without any converging and dispersing such as wide-narrow-wide confinements[32].

Our results showed a clear pattern: migration velocity increased significantly when cells transitioned from the wide section (Wide1) into the narrow section (Narrow) and then decreased as the cells expanded back

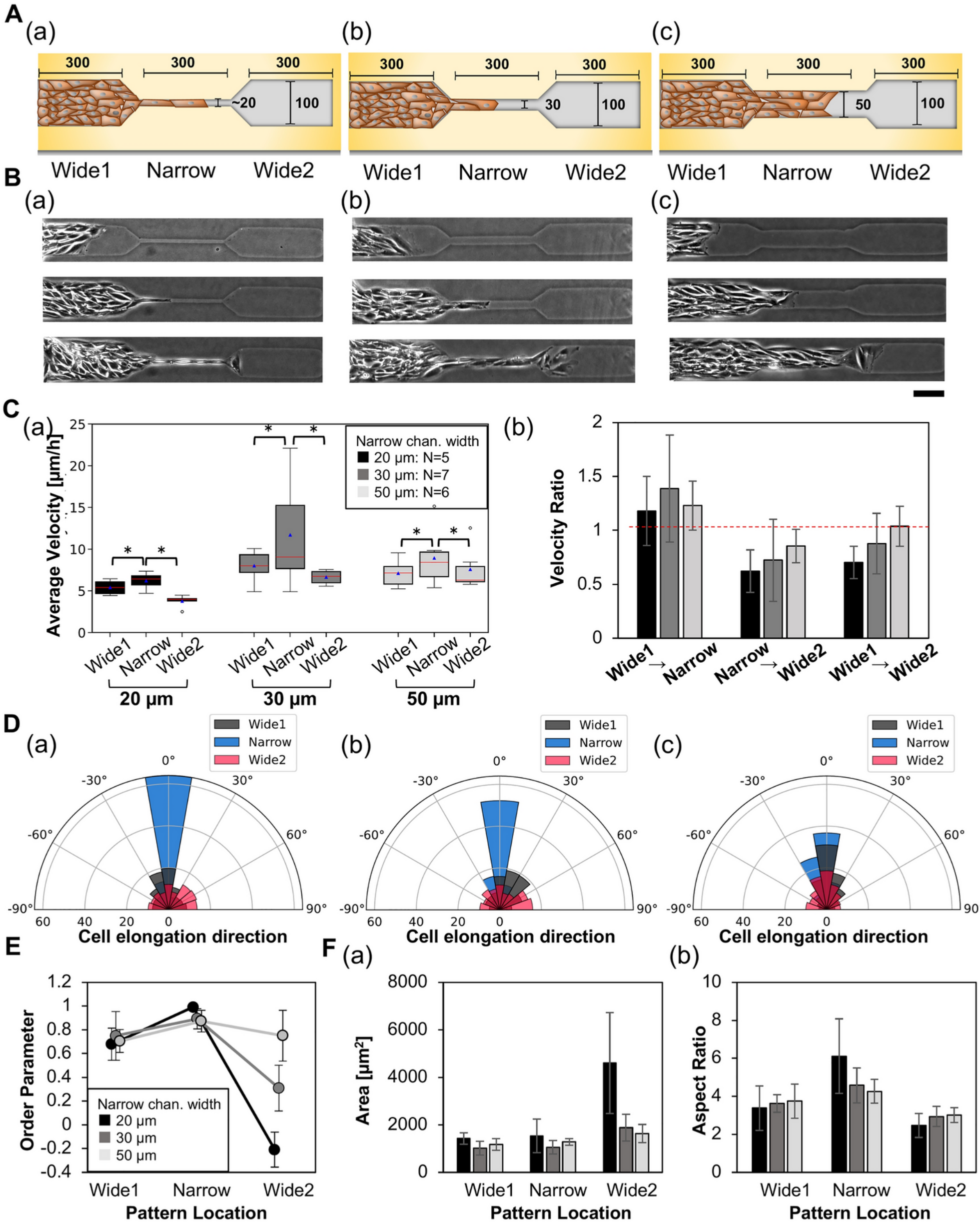

into the wider section (Wide2)(Fig.4 **C**). The largest increase in migration velocity was observed inside the microchannel of 30µm, which is consistent with a previous study indicating that a peak velocity was observed around 30µm[32]. This acceleration during narrowing suggests that the compression induced by the narrowing space modulates cell-cell interactions, potentially optimizing the protrusion dynamics regulated by CIL.

To further scrutinize the dynamic changes in migration velocity observed during the transitions between different widths in wide-narrow-wide confinement, cell elongation direction analysis (Fig.4 **D**), ordering state analysis (Fig.4 **E**), and cell shape analysis were conducted (Fig.4 **F**). The elongation direction increases in all narrow channel widths, where 20µm demonstrated the greatest change, whereas 50µm demonstrated the least increase, which is in agreement with intuitive senses as cells will spontaneously adjust their shape and sizes according to the limited space imposed by the walls of the narrower microchannels, especially when they are restricted by single-cell wide (30µm) or less (20µm). This elongation likely reflects the cells' adjustment to the limited space, where protrusions were restricted to the direction of migration, in line with CIL mechanisms.

The ordering state (Fig.4 **E**) increased significantly within the narrow sections, consistent with the reduced degrees of freedom for directional movement under confinement. This ordering supports the idea that CIL and spatial confinement work in tandem to promote aligned, collective migration. However, upon re-expansion into the wider region, the ordering state decreased sharply, particularly in the 20µm, as cells attempted to protrude in multiple directions, losing the alignment they had in the narrow section. A similar loss of order upon re-expansion has been reported in both experimental and theoretical studies of confined collective migration[39], which demonstrate that geometric constraints enhance alignment, whereas expansion into wider regions disrupts it. This loss of order aligns with the idea that lateral interactions and confinement regulate the cells' orderly behavior, which breaks down when these constraints are relaxed.

◀**Fig. 4**. The effects of different narrow width passage on collectively cell dynamics and ordering. (**A**) Illustrations of the microfabricated patterns on agarose coating for inducing cell invasion. The wide sections are controlled to be 100μm, whereas the narrow channel widths are (**a**) 20μm, (**b**) 30μm, and (**c**) 50μm. The first and last wide channels are distinguished as "Wide1" and "Wide2", respectively. The narrow sections of the pattern are identified as "Narrow (N)" throughout the graphical representations. (**B**) The phase contrast images of migrating cells inside the patterns of (**a**) 20μm, (**b**) 30μm, and (**c**) 50μm narrow channel widths. Top, middle, and bottom: The border of the front cells migrated into Wide1, Narrow, and Wide2 sections, respectively (see Fig. S3 for velocity vector tracks of those migrating cells). (**C**) The sheet expansion velocity for the 20μm (N=5), 30μm (N=7), and 50μm (N=6) narrow channel patterns. (**a**) The migration velocity of the cell sheet inside each section in the wide-narrow-wide patterns. Box plots of the collective cell migration velocity inside each channel were generated to delineate the effects of the narrowing and widening visually. (**b**) The velocity ratio when comparing the migration velocity at each section of the wide-narrow-wide micropattern. Here, Wide1 and Wide2 are included to compare the migration velocity despite not having a direct transition between the two sections. The former label before the arrow is the denominator, and the latter is the numerator (for example, Wide1 to Wide2 means Wide1 is taken as the denominator and Wide2 as the numerator when obtaining the ratio. Left, middle and right bars represent the ratio of 20μm, 30μm, and 50μm narrow section patterns, respectively. The red dashed line is the reference value for visualizing whether the transition increased or decreased the migration velocity. Columns above the line indicate an increase in migration velocity, whereas any columns below the red dashed line indicate a decrease in migration velocity. (**D**) The polar histograms representing the directionality analysis of the cells inside the wide-narrow-wide patterns with (**a**) 20μm, (**b**) 30μm, and (**c**) 50μm width narrow sections. (**E**) The order parameter analysis of the cell migration velocity vectors of the cells inside the wide-narrow-wide patterns with (**a**) 20μm, (**b**) 30μm , and (**c**) 50μm width narrow sections. (**F**) The cell shape ((**a**) Cell area, and (**b**) cell aspect ratio) comparisons between cells inside the wide-narrow-wide patterns. Left, middle and right bars represent the ratio of 20μm, 30μm, and 50μm narrow section patterns, respectively. *P < 0.05.

Moreover, the changes in cell shape corroborate these findings. As shown in Fig.4 **F**(a), cell area increased as cells exited the narrow region and entered the wider space, and their aspect ratio (Fig.4 **F**(b)) decreased accordingly. In particular, cells in the 20μm channel exhibited a three-fold increase in surface area upon expansion, further supporting the notion that cells lose directional control when they are no longer confined. The sharp decrease in the ordering state and changes in cell shape indicate that cells attempt to expand in all available directions once they enter the wider section, reflecting the loss of confinement-driven alignment.

Width dependence of propagation velocity in gradual wide-narrow-wide confinement structure

To investigate whether the observed changes in collective cell ordering resulted from abrupt confinement transitions or simply the geometric properties, we examined cell behavior in a gradually altering confinement structure. Previous studies have explored how gradual confinement transitions influence collective migration, showing that cells adjust their migration velocity and alignment in response to spatial constraints[39,40]. A theoretical model has predicted that migration velocity changes under gradual confinement follow a conservation of flux principle, similar to a Bernoulli-like effect[39]. While their work provided key theoretical insights into velocity modulation under spatial constraints, our study experimentally examines migration velocity changes in a continuous constriction-expansion geometry while also considering collective order and cellular morphology. By analyzing how cell shape and alignment contribute to migration behavior, we aim to provide additional context to confinement-driven migration dynamics.

Figures 5 **A** and **B** show the schematics and micrographs of the gradual wide-narrow-wide confinement. Similar to the stepwise results, migration velocity showed a relationship with confinement width: as the channel narrowed, migration velocity increased and decreased during expansion (Fig. 5 **C**)(N=5). Interestingly, unlike in the stepwise experiment, the order parameter did not sharply drop after expansion from the narrow region. Instead, the cells maintained their alignment, preserving the ordered state throughout the structural transitions (Fig. 5 **D**). This suggests that gradual confinement changes allow cells to retain their coordination, possibly by avoiding the abrupt disruption of cell-cell interactions seen in the stepwise experiment.

The observed behavior aligns with findings from the T-shape branching experiment, where CIL and CFL played a critical role in guiding cell movement. In the narrow regions, where cells were compressed, CIL likely promoted forward-directed protrusions, accelerating migration as cells maintained tight coordination. In contrast, upon entering the wider sections, the weakening of CIL-mediated protrusions may have led to more dispersed movement. However, in the gradual confinement experiment, the cells avoided the sharp breakdown in order observed in the stepwise experiment, possibly because lateral interactions, regulated by CFL, were less disrupted by the gradual transitions in confinement.

Morphological changes in the cells mirrored those seen in the stepwise wide-narrow-wide transitions. As shown in Fig. 5 **E**, cell area increased as the channel expanded, accompanied by a decrease in aspect ratio (Fig. 5 **F**). These changes in cell shape suggest that, as in the T-shape experiment, cells adjusted their protrusions and alignment based on the availability of space, expanding in multiple directions as confinement lessened. Despite these morphological changes, the collective cell dynamics remained robust, with the ordering behavior largely preserved.

We extended our investigation to three-dimensional (3D) structures to explore how these principles might apply to more physiologically relevant environments. To study vascular endothelial cells (ECs) during

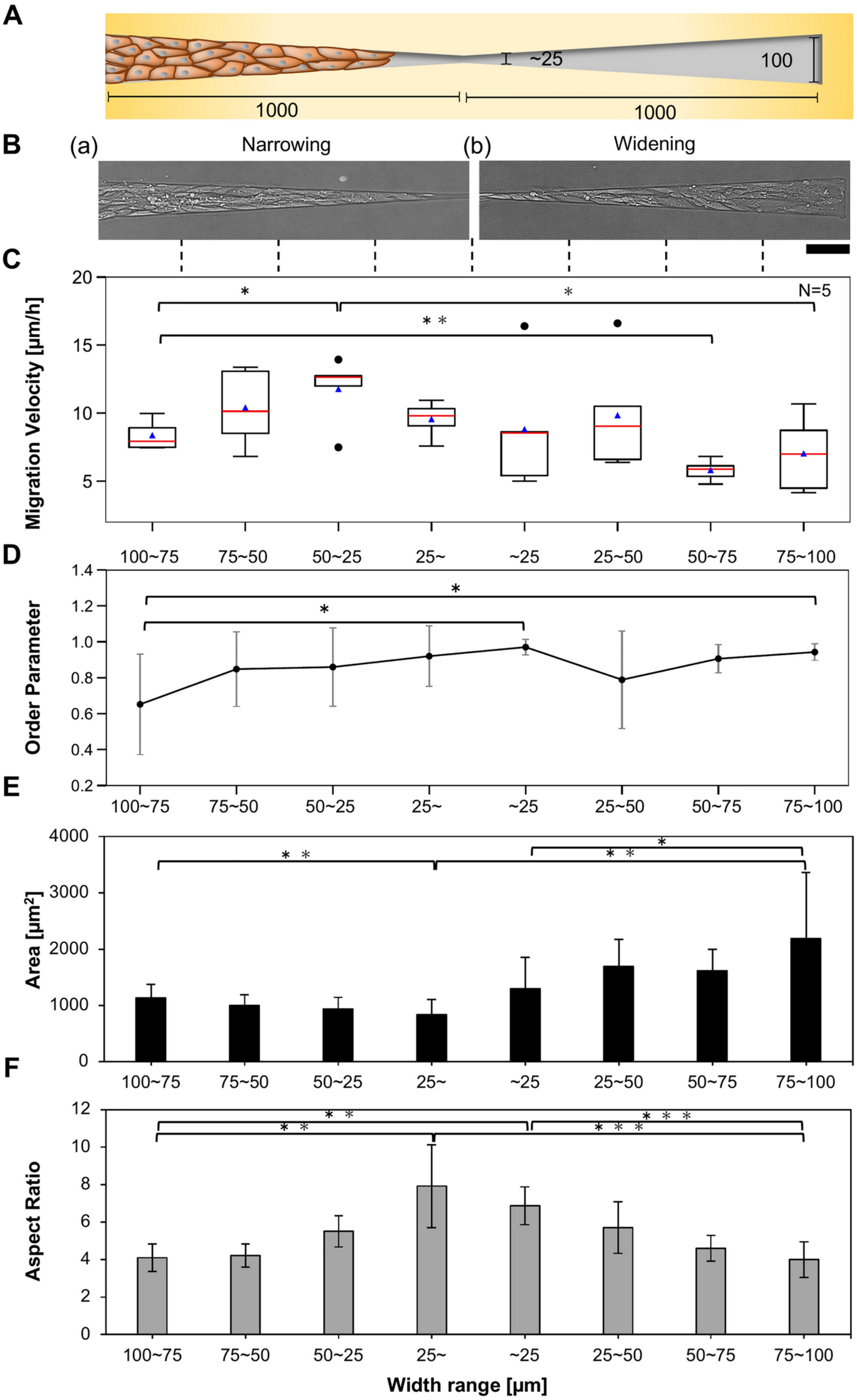

Fig. 5. The collective dynamics and cell shape analysis results of collective cell migration inside gradually width-changing micropattern. (**A**) Illustration of gradually width-changing micropattern fabricated on the agarose coating. The shape was made symmetrical, where the widest section at each end of the micropattern was designed to have 100µm and the narrow sections to be less than 25µm. (**B**) The micrographs of the endothelial cells inside the geometrical confinement: Left, narrowing part; right, widening part. Bar, 100µm (see Fig. S3 for velocity vector tracks of those migrating cells). (**C**) The migration velocity at different sections of the micropattern (N=5). (**D**) The order parameter analysis of the velocity vectors at the corresponding sections of the micropattern. (**E**) The column graphs represent the results of the cell area analysis at each section of the pattern. (**F**) The corresponding aspect ratio analysis of the cells. *P < 0.05, **P < 0.01, ***P < 0.001.

angiogenesis within flexible 3D confinements, we developed a novel method to fabricate capillary microtunnels in gelatin gel[41]. This method involves an on-chip photo-thermal 3D gelatin-gel microfabrication system, which uses a focused, water-permeable 1064-nm infrared laser for spot heating on a platinum-coated microneedle tip, combined with a motorized XY stage for precise positioning (Fig. S4 **A**). By adjusting the laser intensity and position, micrometer-sized spot heating melts the surrounding gelatin gel, allowing the creation of confined microtunnels.

Using this technology, we cultivated MS-1 cells in 3D inverted bicone microtunnels, mimicking capillary structures. Initially, MS-1 cells proliferated on the outer surface of the gelatin block, eventually migrating into the microtunnel to form a lumen structure (Figs. S4 **B**-**D**). As the cell sheet progressed, the inner diameter of the microtunnel decreased, causing a transition from a luminal monolayer to a clustered structure (Figs. S4 **E**-**F**). Interestingly, as the inner diameter increased again, the cluster reverted to a luminal structure reflecting a dynamic response to spatial constraints when the diameter reached approximately the same size as when clustering initially occurred. This transition occurred consistently across samples (N=13), with transition diameters ranging from $12\mu m$ to $38\mu m$ (Figs. S4 **G**).

Discussion

The results from our experiments reveal a multi-faceted mechanistic basis for collective cell migration within confined structures, highlighting the influence of spatial constraints on cellular interactions, movement patterns, and structural organization. Firstly, at the leading edge, front cells in single-cell trains do not strongly attract rear cells through contact following locomotion (CFL). Instead, rear cells migrate based on space availability—preferentially entering vacant branches but, when both branches are occupied, moving in opposite directions, suggesting a repulsive or space-filling behavior. Secondly, the mean migration velocity remains stable across branching and reassembly as long as the overall confinement width is maintained. However, velocity fluctuations increased in single-cell trains, emphasizing the role of lateral interactions in maintaining steady migration behavior. Lastly, the order parameter, a measure of directional alignment, was maintained only when the widths of the channels allowed for multiple lateral cell interactions, such as in wider channels (i.e. $50\mu m$ narrow channel in the wide-narrow-wide pattern) and when the transition was gradual. In narrower branches, the order parameter decreased after exiting from narrow restricted areas, reflecting the loss of directional coordination in the absence of lateral interactions.

The presence of CIL to a certain degree, as observed in our T-shaped branching experiment, suggests that cell-to-cell interactions within narrow confinements discourage direct following behaviors. Here, rear cells often diverge from the path of preceding cells, indicating that spatial constraints are instrumental in shaping directional choices rather than purely follower-leader dynamics. This behavior is likely a response to environmental cues rather than active signaling, as rear cells appear to prioritize unoccupied pathways over direct cell-to-cell following. The observed fragmentation behavior caused by the repolarization from the junction point agrees with a recent study on confined MDCK epithelial cells where CIL-like interaction is a boundary phenomenon that controls cluster sizes and polarity by reducing them[42]. In contrast, the difference in behavior observed with NRK-52E epithelial cells may be a result of cell species, the micropattern geometry, or the presence of leader-like phenotype edge[36]. Moreover, Gov's group applied the universal coupling between cell speed and persistence (UCSP) model[43], which describes how contact interactions influence internal polarization and collective migration in one-dimensional single-cell-wide trains[44]. Their findings suggest that the balance between contact inhibition of locomotion (CIL) and cryptic lamellipodia governs these behaviors, with larger noise disrupting polarity and stability. If confinement at the T-junction amplifies noise in single-cell trains, it may explain the observed experimental results.

A key finding of this study was that the migration velocity of the cell sheet remained largely unchanged, even when cell trains were divided into narrow, single-cell-wide pathways. This robustness, maintained as long as the total pathway width was conserved, suggests a self-regulation mechanism that preserves collective cell speed, likely essential for endothelial cells navigating confined environments, such as blood vessels. This aligns with previous *in vivo*observations in Xenopus neural crest cells, where an optimal geometry size was identified for a given cluster[34]. While average migration velocity remained stable, fluctuations in velocity increased during division, particularly in single-cell-wide pathways, likely due to disrupted coordination from reduced lateral interactions. Fluctuations decreased after reassembly, suggesting that lateral interactions helped restore uniform migration for both front and rear cells. Similar confinement-induced fluctuations have been widely reported; epithelial cells in narrow channels exhibit increased fluctuations due to constraints on intercellular coordination and force transmission[33], and geometric confinement has been shown to amplify migration variability, which diminishes upon expansion into wider regions[39]. Although this study does not explicitly assess intermittent migration, the observed fluctuation dynamics align with these prior findings, highlighting the role of spatial constraints in regulating collective behavior.

Additionally, in our stepwise and gradual wide-narrow-wide patterns, we observed that spatial compression accelerates cell movement, potentially by adjusting the cell-to-cell interaction distance in a way that strengthens protrusion mechanisms. In narrower sections, CIL likely drives cells to compress and increase forward protrusions, thereby increaseing order and boosting migration speed. When the geometry is excessively narrow, however, the cells become elongated and do not have the adhesive area necessary to generate lamellipodial protrusion which causes the velocity to decrease. A previous study examined single-cell migration in a similar wide-narrow-wide confinement pattern, focusing on nuclear deformation driven by perinuclear actin polymerization. In that study, a significant reduction in cell velocity was observed when the narrow region was $\leq 2\mu m$ wide, regardless of its length ($5\mu m$ to $20\mu m$), due actin-driven nuclear engagement and deformation[45]. However, in our study, the narrowest region is at least $10\mu m$, and there is no top barrier to apply external pressure on the cells. Therefore, nuclear deformation is unlikely to play a role under our current experimental conditions. Our observation is in accordance with prior studies of the single-cell interaction with the substrate geometry size[35]and collective cell migration inside confinement strips[32]. Conversely, as cells enter wider areas, the weakening of confinement and available open space may reduce forward protrusion strength, allowing cells to expand and migrate in multiple directions, leading to decreased alignment. The ordering behavior is consistent with previous observations in both two-dimensional channels[32,33,46]and three-dimensional microtubular structures[47,48]. This behavior is corroborated by the increase in cell surface area observed when cells re-enter the wider region. The cell aspect ratio decrease induced by the widening of confinement space has also been previously observed[35]. The cells' expansion mirrors their behavior in the T-shaped branching pattern, where protrusions extend toward available open space, reflecting a loss of directional control once the lateral confinement weakens.

Interestingly, in the stepwise branching and wide-narrow-wide pattern, the order parameter after switching from the narrow phase decreased more than the original wide section having the same geometrical parameter. This indicates that the past cellular state inside confinement can influence the future behavior of the cells, which is a consideration oftentimes neglected in simulations that attempts to observe cellular behavior inside a specific topology. In contrast, gradual transitions preserved order within the cell cohort, even when the confinement expanded. These findings suggest that confinement geometry influences both CIL and CFL, with the latter helping maintain cell coordination during more gradual changes in space. While our study primarily focuses on the collective migration dynamics of confined cell sheets, nematic order in cell shapes may also play a role in the observed behaviors. Recent studies have highlighted the emergence of nematic ordering and its impact on collective flows in multicellular systems, with topological defects influencing the organization and migration patterns of cells[49]. Although we did not directly measure nematic order in this study, future investigations could explore its potential contribution to cell alignment and directional persistence in confined migration.

In 3D confinement experiments (Fig. S4), the observed reversible transitions between luminal and clustered states further underscore the mechanistic influence of confinement geometry. These transitions, governed by the tunnel diameter, mirror the 2D behavior of cells adapting to available space by reorganizing collectively. The reversibility suggests that structural shifts, like the shift between luminal and clustered forms, are induced by spatial constraints rather than biochemical signals alone. This mechanistic response to environmental geometry may be essential for processes such as tissue remodeling, where cells encounter topographical changes. This geometry-sensitive behavior aligns with previous findings in epithelial tube structures, where the thickness of luminal epithelial sheets has been shown to depend on tube diameter. Specifically, Wang et al. demonstrated that in smaller tubes, epithelial cells form thicker luminal structures, with cell height reaching up to $8\mu m$ at a diameter of $25\mu m$[47]. As tube diameter increases, the luminal sheet becomes thinner due to reduced mechanical constraints. This suggests that confinement regulates the structural adaptation of epithelial tissues, a principle that is also evident in our 3D microtunnel experiments. Furthermore, recent studies on MDCK cell monolayers confined within cylindrical curved surfaces have demonstrated that collective rotational migration is also geometry-sensitive: migration velocity peaks at $100\mu m$ tube diameter, while rotational migration ceases in tubes wider than $150\mu m$[48]. Thus, the findings across both 2D and 3D experiments collectively illustrate how endothelial cells adapt to confined environments, using physical constraints as a guide for collective migration.

While this study provides new insights into the impact of confinement geometry on collective cell migration, several limitations should be acknowledged. First, our experiments were conducted within controlled two-dimensional (2D) and three-dimensional (3D) microenvironments with well-defined confinement structures. Although these conditions allowed us to observe behaviors driven by spatial constraints, they may not fully replicate the complex and dynamic environments that cells experience *in vivo*. *In-vivo* biological environments feature additional variables, such as extracellular matrix (ECM) heterogeneity, gradient-based chemotaxis, and varying degrees of mechanical stiffness, which could influence cell behavior in ways not captured here. Future studies could incorporate ECM components or adjustable mechanical properties within the confinement structures to better mimic *in vivo* conditions and explore their effects on migration dynamics.

Additionally, while we investigated cell-to-cell interactions through confinement-induced CIL and CFL, we did not specifically examine the underlying molecular pathways involved in these behaviors. Mechanisms such as Rac1 activation and other signaling pathways have been implicated in cell migration and protrusion dynamics, and exploring these pathways could reveal more about the regulation of migration under confined conditions. Future research could employ fluorescent markers or live-cell imaging of key signaling molecules to directly assess their roles in CIL, CFL, and other cell behaviors within confined environments. In our 3D experiments, we successfully observed transitions between luminal and clustered states, but further investigation is needed to understand the underlying physical and cellular factors driving these transitions. The exact role of confinement geometry, cell density, and mechanical properties in promoting or inhibiting these structural changes remains unclear. Future studies could systematically vary tunnel diameter, ECM stiffness, and cell density to isolate the key drivers of these transitions. Additionally, by introducing chemotactic gradients within 3D tunnels, we could explore how chemical cues interact with physical confinement to direct collective migration, which would be especially relevant to understanding processes like angiogenesis and metastasis.

Finally, while the current study focused on endothelial cells, extending this work to other cell types, such as epithelial or cancer cells, would allow us to evaluate whether the observed behaviors are specific to endothelial cells or represent general principles of collective migration under confinement. Cancer cells, for instance, are known to migrate through confined spaces during metastasis, often adapting their migration strategies in response to physical barriers[50]. Investigating how different cell types respond to identical confinement conditions could uncover cell-type-specific migration strategies, providing valuable insights for targeted therapeutic approaches.

Methods

Cells

In this study, we utilized a mouse-derived endothelium-like cell line, MILE SVEN 1 (MS-1; CRL-2279, ATCC, Manassas, VA, USA). The cells were maintained at $37^{\circ}C$ in a humidified incubator with 5% CO_2, using Dulbecco's Modified Eagle's Medium (DMEM; Gibco, Thermo Fisher Scientific, Waltham, MA, USA) supplemented with 10% heat-inactivated fetal bovine serum (FBS; Gibco, Thermo Fisher Scientific, Waltham, MA, USA) and 100 U/mL penicillin-streptomycin (Gibco, Thermo Fisher Scientific, Waltham, MA, USA). The subculture cycle was maintained at approximately 4–6 days. Cells used for experiments were detached from the culture surface using Trypsin-EDTA solution (Gibco, Thermo Fisher Scientific, Waltham, MA, USA). After aspirating the culture medium, cells were rinsed once with phosphate-buffered saline (PBS) to remove residual serum, followed by the addition of Trypsin-EDTA. The dish was incubated at $37^{\circ}C$ for 2–3 minutes until the cells detached. The detached cells were neutralized with DMEM containing 10% FBS, collected, and centrifuged at 200 × g for 5 minutes. The pellet was then resuspended in fresh medium for subsequent experiments.

A 1064/1480-nm laser photo-thermal microfabrication system

A 1064/1480-nm laser photo-thermal microfabrication system was employed to fabricate agarose microstructures, building on methodologies detailed in prior reports[32,51]. The system integrates a laser emitting module (PYL-1–1064-M, IPG Laser GmbH, Burbach, Germany; RLM-1–1480, IPG Laser, Oxford, MA, USA) with an inverted bright-field microscope (IX70, x20 obj. PLAN Apo, Olympus, Tokyo, Japan) for precision laser application.

Control of the 1480-nm laser beam was achieved through a shutter controller (FSH-C, SIGMA KOKI, Tokyo, Japan), which can be operated manually or automated via a LabVIEW®-powered software interface. To facilitate microfabrication, the agarose-coated culture dish was mounted on a motorized X-Y microscope stage (SIGMA KOKI CO., LTD., Tokyo, Japan) governed by a feedback stage controller (FC-101B, SIGMA KOKI CO., LTD., Tokyo, Japan). The stage's position could also be fine-tuned manually with a joystick controller (FJ-401B, SIGMA KOKI, Tokyo, Japan), enabling adaptable and accurate adjustments throughout the process.

Agarose microstructure fabrication on cultivation dish

To prepare a non-adhesive agarose layer, a 35m tissue culture dish (AGC TECHNO GLASS, Shizuoka, Japan) was coated with a 3.0 wt% agarose gel (low melting, analytical grade; Promega, Madison, WI, USA). The dish surface was initially treated with a plasma etching device (PIB-20, Vacuum Device, Ibaraki, Japan) for 5 minutes at a discharge current of 30mA under 13.3Pa pressure, enhancing its hydrophilicity. A thin and uniform agarose gel layer was formed by spinning sol-state agarose droplets using a spin coater (IH-D7, MIKASA, Tokyo, Japan) at 500 rpm for 3 seconds, followed by 3,000 rpm for 18 seconds. After coating, the dish was left to dry for 10 minutes before being refrigerated for 1 hour. Following refrigeration, distilled water was added for storage, making the dish ready for subsequent microfabrication. During agarose microfabrication, the distilled water or culture medium in the dish absorbs laser energy at the irradiated focal point, locally heating and dissolving the thin agarose gel layer at the laser spot. By adjusting the intensity of the laser, the dimensions of the adhesive regions can be precisely controlled, enabling tailored microfabrication designs.

Cell cultivation in agarose microstructures

A reservoir chamber measuring 0.5m in width and 2m in length was fabricated as an agarose-free region within a thin agarose layer on a culture dish, utilizing a 1064/1480-nm laser photo-thermal microfabrication technique. The dish was washed three times with DMEM medium to remove debris and filled with 2mL of fresh DMEM to support cell cultivation. Subsequently, approximately 3×10^4 MS-1 cells were seeded onto the dish and incubated at $37^{\circ}C$ in a humidified atmosphere containing 5% CO_2. After approximately one hour of incubation, cells located within the agarose-free reservoir chamber adhered firmly to the dish surface, while those over the agarose-coated regions remained suspended in the medium. These unattached cells were removed during a medium exchange with fresh DMEM. The dimensions of the reservoir chamber were specifically chosen to allow multiple microchannels to be fabricated along its edge, ensuring that cells migrating into these channels originated from the same population. This design also provided sufficient spacing between channels to prevent cross-channel interactions. When the cells in the reservoir chamber reached near confluency, microchannels were created in the adjacent agarose layer using the photo-thermal microfabrication system to guide cell migration. Once MS-1 cells began entering the microchannels, time-lapse imaging was initiated to track their collective invasion dynamics.

Time-lapse recording and analysis of cellular dynamics

Time-lapse of every 10-min interval images of the cells inside the topographical constraints were taken by two systems: the agarose microfabrication system equipped with a stage-top microscope incubation system (TOKAI HIT, Shizuoka, Japan), motorized X-Y microscope stage for software controlled capturing location shifts, and a scientific CCD camera (1501M-GE-TE, Thorlabs, USA), as well as an automated image recording system, CytoWatcher (WSL-1800, Atto Ltd., Tokyo, Japan). The temperature during the timelapse observation was controlled to be $37^{\circ}C$ and the same pH as the growth medium inside the incubator with the setting mentioned previously. The pH was regulated by employing a gas mixer (KOFLOC KOJIMA INSTRUMENTS INC., Tokyo, Japan) to combine air and CO_2 gas which was then filtered and emitted into the water bath of the stage-top microscope incubation system through a tube. The cellular dynamics and morphological parameters such as cell area and aspect ratios were analyzed using Java language-based image processing program ImageJ (NIH, Bethesda, MD, USA) by tracking the change in cell sheet position for velocity (using every 1-hour interval images) and segmenting the cells for delineating morphological changes. The migration velocity of the cell sheet was determined by manually defining its boundary and tracking the displacement of its center of mass (CoM) over time using ROI management in ImageJ (Fig. S5 **A**). Rather than using the entire channel as an ROI, the analysis focused on a defined region surrounding the migrating cell sheet at each time point. Velocity measurements were taken at 1-hour intervals by calculating the CoM displacement of the defined boundary. To approximate the displacement of the leading edge, the migration velocity **V** was determined as $\mathrm{V} = (\Delta CoM/\Delta t) \times 2$ (see Fig. S5 **B**). After calculating the migration velocity, the data was smoothed by applying a moving average, where each velocity value was averaged with the two preceding and two succeeding time points. The velocity was calculated from the time the cells entered the channel of interest until they reached the endpoint of the channel. Since the migration speed varied, the number of velocity values obtained per channel differed between experiments. To quantify the alignment of cell migration directions, the order parameter was calculated by comparing the velocity vectors of neighboring cells relative to the overall migration direction. Cells were manually segmented and further refined using an automated segmentation method to extract individual cell boundaries. The velocity vector for each cell was determined from the center of mass displacement over time. These velocity vectors were plotted using a custom Python program. The order parameter was then computed as the cosine of the angle between each cell's velocity vector and the mean migration direction, providing a measure of collective motion coherence.

Statistical analysis

All statistical analyses of propagation velocities and fluctuation CV are expressed as mean ± standard deviation (S.D.) based on 1-hour interval recordings unless otherwise specified. Differences among groups for migration velocity and fluctuation CV were analyzed using one-way analysis of variance (ANOVA), followed by pairwise t-tests for post hoc comparisons. Welch's t-test was used for non-parametric sample comparison. Statistical significance was set at $P<0.05$ for one *, $P<0.01$ for two **, and $P<0.001$ for three ***. All statistical analyses were carried out using Python.

Data availability

The datasets used and analyzed during the current study are available from the corresponding author upon reasonable request.

Received: 25 December 2024; Accepted: 5 March 2025

References

1. Friedl, P. & Gilmour, D. Collective cell migration in morphogenesis, regeneration and cancer. *Nat. Rev. Mol. Cell Biol.* **10**, 445–457. https://doi.org/10.1038/nrm2720 (2009).
2. Rørth, P. Collective Cell Migration. *Annu. Rev. Cell Dev. Biol.* **25**, 407–429. https://doi.org/10.1146/annurev.cellbio.042308.113231 (2009).
3. Mishra, A. K., Campanale, J. P., Mondo, J. A. & Montell, D. J. Cell interactions in collective cell migration. *Development (Cambridge)* **146**, 1–7. https://doi.org/10.1242/dev.172056 (2019).
4. Haeger, A., Wolf, K., Zegers, M. M. & Friedl, P. Collective cell migration: Guidance principles and hierarchies. *Trends in Cell Biology* **25**, 556–566. https://doi.org/10.1016/j.tcb.2015.06.003 (2015).
5. Khalil, A. A. & de Rooij, J. Cadherin mechanotransduction in leader-follower cell specification during collective migration. *Experimental Cell Research* **376**, 86–91. https://doi.org/10.1016/j.yexcr.2019.01.006 (2019).
6. Farooqui, R. & Fenteany, G. Multiple rows of cells behind an epithelial wound edge extend cryptic lamellipodia to collectively drive cell-sheet movement. *Journal of Cell Science* **118**, 51–63. https://doi.org/10.1242/jcs.01577 (2005).
7. Rottner, K. & Schaks, M. Assembling actin filaments for protrusion. *Current Opinion in Cell Biology* **56**, 53–63. https://doi.org/10.1016/j.ceb.2018.09.004 (2019).
8. Cai, D. et al. Mechanical feedback through E-cadherin promotes direction sensing during collective cell migration. *Cell* **157**, 1146–1159. https://doi.org/10.1016/j.cell.2014.03.045 (2014).
9. Arima, S. et al. Angiogenic morphogenesis driven by dynamic and heterogeneous collective endothelial cell movement. *Development* **138**, 4763–4776. https://doi.org/10.1242/dev.068023 (2011).
10. Herbert, S. P. & Stainier, D. Y. Molecular control of endothelial cell behaviour during blood vessel morphogenesis. *Nature Reviews Molecular Cell Biology* **12**, 551–564. https://doi.org/10.1038/nrm3176 (2011).
11. Gerhardt, H. et al. VEGF guides angiogenic sprouting utilizing endothelial tip cell filopodia. *Journal of Cell Biology* **161**, 1163–1177. https://doi.org/10.1083/jcb.200302047 (2003).
12. Bao, P. *et al.* The Role of Vascular Endothelial Growth Factor in Wound Healing. *Journal of Surgical Research* **153**, 347–358, https://doi.org/10.1016/j.jss.2008.04.023 (2009). NIHMS150003.
13. Ziyad, S. & Iruela-Arispe, M. L. Molecular Mechanisms of Tumor Angiogenesis. *Genes and Cancer* **2**, 1085–1096. https://doi.org/10.1177/1947601911432334 (2011).
14. Claesson-Welsh, L., Dejana, E. & McDonald, D. M. Permeability of the Endothelial Barrier: Identifying and Reconciling Controversies. *Trends in Molecular Medicine* **27**, 314–331. https://doi.org/10.1016/j.molmed.2020.11.006 (2021).
15. Mayor, R. & Etienne-Manneville, S. The front and rear of collective cell migration. *Nature Reviews Molecular Cell Biology* **17**, 97–109. https://doi.org/10.1038/nrm.2015.14 (2016).
16. Trepat, X. et al. Physical forces during collective cell migration. *Nature Physics* **5**, 426–430. https://doi.org/10.1038/nphys1269 (2009).
17. Yamaguchi, N., Mizutani, T., Kawabata, K. & Haga, H. Leader cells regulate collective cell migration via Rac activation in the downstream signaling of integrin β1 and PI3K. *Scientific Reports* **5**, https://doi.org/10.1038/srep07656 (2015).
18. Omelchenko, T., Vasiliev, J. M., Gelfand, I. M., Feder, H. H. & Bonder, E. M. Rho-dependent formation of epithelial "leader" cells during wound healing. *Proceedings of the National Academy of Sciences of the United States of America* **100**, 10788–10793. https://doi.org/10.1073/PNAS.1834401100 (2003).
19. MacHacek, M. et al. Coordination of Rho GTPase activities during cell protrusion. *Nature* **461**, 99–103. https://doi.org/10.1038/NATURE08242 (2009).
20. Reffay, M. et al. Orientation and Polarity in Collectively Migrating Cell Structures: Statics and Dynamics. *Biophys. J.* **100**, 2566–2575. https://doi.org/10.1016/j.bpj.2011.04.047 (2011).
21. Wang, X., He, L., Wu, Y. I., Hahn, K. M. & Montell, D. J. Light-mediated activation reveals a key role for Rac in collective guidance of cell movement in vivo. *Nature Cell Biology* **12**, 591–597. https://doi.org/10.1038/ncb2061 (2010).

22. Caussinus, E., Colombelli, J. & Affolter, M. Tip-Cell Migration Controls Stalk-Cell Intercalation during Drosophila Tracheal Tube Elongation. *Current Biology* **18**, 1727–1734. https://doi.org/10.1016/J.CUB.2008.10.062/ATTACHMENT/F83DB115-E333-4B80-9EFF-4E227FB93C5F/MMC14.MOV (2008).
23. Jakobsson, L. et al. Endothelial cells dynamically compete for the tip cell position during angiogenic sprouting. *Nature Cell Biology* **12**, 943–953. https://doi.org/10.1038/ncb2103 (2010).
24. Campanale, J. P. & Montell, D. J. Who's really in charge: diverse follower cell behaviors in collective cell migration. *Curr. Opin. Cell Biol.* **81**, 102160. https://doi.org/10.1016/J.CEB.2023.102160 (2023).
25. Lebreton, G. & Casanova, J. Specification of leading and trailing cell features during collective migration in the Drosophila trachea. *J. Cell Sci.* **127**, 465–474. https://doi.org/10.1242/JCS.142737/VIDEO-3 (2014).
26. Bianco, A. *et al.* Two distinct modes of guidance signalling during collective migration of border cells. *Nat. 2007 4487151* **448**, 362–365, https://doi.org/10.1038/nature05965 (2007).
27. Prasad, M. & Montell, D. J. Cellular and Molecular Mechanisms of Border Cell Migration Analyzed Using Time-Lapse Live-Cell Imaging. *Dev. Cell* **12**, 997–1005. https://doi.org/10.1016/j.devcel.2007.03.021 (2007).
28. Vishwakarma, M. *et al.* Mechanical interactions among followers determine the emergence of leaders in migrating epithelial cell collectives. *Nature Communications 2018 9:1* **9**, 1–12, https://doi.org/10.1038/s41467-018-05927-6 (2018).
29. Rossetti, L. *et al.* Optogenetic generation of leader cells reveals a force–velocity relation for collective cell migration. *Nature Physics* **20**, https://doi.org/10.1038/s41567-024-02600-2 (2024).
30. Ilina, O. et al. Cell–cell adhesion and 3D matrix confinement determine jamming transitions in breast cancer invasion. *Nature Cell Biology* **22**, 1103–1115. https://doi.org/10.1038/s41556-020-0552-6 (2020).
31. Law, R. A. *et al.* Cytokinesis machinery promotes cell dissociation from collectively migrating strands in confinement. *Science Advances* **9**, https://doi.org/10.1126/sciadv.abq6480 (2023).
32. Sentoku, M., Hashimoto, H., Iida, K., Endo, M. & Yasuda, K. Photothermal agarose microfabrication technology for collective cell migration analysis. *Micromachines* **12**, 1015. https://doi.org/10.3390/MI12091015 (2021).
33. Vedula, S. R. K. et al. Emerging modes of collective cell migration induced by geometrical constraints. *Proceedings of the National Academy of Sciences of the United States of America* **109**, 12974–12979. https://doi.org/10.1073/pnas.1119313109 (2012).
34. Szabó, A. et al. In vivo confinement promotes collective migration of neural crest cells. *Journal of Cell Biology* **213**, 543–555. https://doi.org/10.1083/jcb.201602083 (2016).
35. Mohammed, D. et al. Substrate area confinement is a key determinant of cell velocity in collective migration. *Nature Physics* **15**, 858–866. https://doi.org/10.1038/s41567-019-0543-3 (2019).
36. Li, D. & Wang, Y.-L. Coordination of cell migration mediated by site-dependent cell-cell contact. *Proceedings of the National Academy of Sciences* **115**, 10678–10683 (2018).
37. Löber, J., Ziebert, F. & Aranson, I. S. Collisions of deformable cells lead to collective migration. *Scientific reports* **5**, 9172 (2015).
38. Marel, A.-K.K. et al. Flow and diffusion in channel-guided cell migration. *Biophysical Journal* **107**, 1054–1064. https://doi.org/10.1016/j.bpj.2014.07.017 (2014).
39. Tarle, V. *et al.* Modeling collective cell migration in geometric confinement. *Phys. Biol.* **14**, https://doi.org/10.1088/1478-3975/AA6591 (2017).
40. Yang, Y. et al. Probing Leader Cells in Endothelial Collective Migration by Plasma Lithography Geometric Confinement. *Sci. Rep.* **6**, 22707. https://doi.org/10.1038/SREP22707 (2016).
41. Sentoku, M., Iida, K., Hashimoto, H. & Yasuda, K. Dominant geometrical factors of collective cell migration in flexible 3d gelatin tube structures. *Biophysical Reports* **2**, https://doi.org/10.1016/j.bpr.2022.100063 (2022).
42. Bertrand, T. *et al.* Clustering and ordering in cell assemblies with generic asymmetric aligning interactions. *Physical Review Research* **6**, 34–38, https://doi.org/10.1103/PhysRevResearch.6.023022 (2024). 2012.00785.
43. Maiuri, P. *et al.* Actin flows mediate a universal coupling between cell speed and cell persistence. *Cell* **161**, 374–386, https://doi.org/10.1016/J.CELL.2015.01.056/ATTACHMENT/D18D1F43-DCA3-4B5A-8C1B-3F4B9554DBAF/MMC7.PDF (2015).
44. Ron, J. E. et al. Polarization and motility of one-dimensional multi-cellular trains. *Biophys. J.* **122**, 4598–4613. https://doi.org/10.1016/J.BPJ.2023.11.003 (2023).
45. Thiam, H. R. et al. Perinuclear Arp2/3-driven actin polymerization enables nuclear deformation to facilitate cell migration through complex environments. *Nature Communications* **7**, 1–14. https://doi.org/10.1038/ncomms10997 (2016).
46. Lin, S.Z., Bi, D., Li, B. & Feng, X.Q. Dynamic instability and migration modes of collective cells in channels. *Journal of the Royal Society Interface* **16**, https://doi.org/10.1098/rsif.2019.0258 (2019).
47. Xi, W., Sonam, S., Saw, T. B., Ladoux, B. & Lim, C. T. Emergent patterns of collective cell migration under tubular confinement. *Nat. Commun.* **8**, 1–15. https://doi.org/10.1038/s41467-017-01390-x (2017).
48. Glentis, A. *et al.* The emergence of spontaneous coordinated epithelial rotation on cylindrical curved surfaces. *Sci. Adv.* **8**, 5406, https://doi.org/10.1126/SCIADV.ABN5406/SUPPL_FILE/SCIADV.ABN5406_MOVIES_S1_TO_S14.ZIP (2022).
49. Yashunsky, V. et al. Chiral Edge Current in Nematic Cell Monolayers. *Physical Review X* **12**, 41017. https://doi.org/10.1103/PhysRevX.12.041017 (2022).
50. Paul, C. D., Mistriotis, P. & Konstantopoulos, K. Cancer cell motility: lessons from migration in confined spaces. *Nature Reviews Cancer* **17**, 131–140. https://doi.org/10.1038/nrc.2016.123 (2017).
51. Moriguchi, H. et al. An agar-microchamber cell-cultivation system: flexible change of microchamber shapes during cultivation by photo-thermal etching. *Lab Chip* **2**, 125–132. https://doi.org/10.1039/b202569h [doi] (2002).

Acknowledgements

We thank Dr. Kazufumi Sakamoto and all the members of Yasuda lab for their technical support, discussion, and suggestions. This research was funded by research and development projects of the Industrial Science and Technology Program, the New Energy and Industrial Technology Development Organization (NEDO, P08030), JSPS KAKENHI Grant (JP22K18955), JST CREST program (1J138), Waseda University Grant for Special Research Projects (2024R-024, 2024C-158).

Author contributions

K.Y. proposed the idea and conceived the experiments, M.S., M.E., M.T. and W.H. conducted the experiments, M.S., M.E., M.T. and K.Y. analyzed the results and discussed, M.S. and K.Y. wrote the manuscript, K.Y. acquired funding. All authors reviewed the manuscript.

Funding

This research was funded by research and development projects of the Industrial Science and Technology Program, the New Energy and Industrial Technology Development Organization (NEDO, P08030), JSPS KAKENHI Grant (JP22K18955), JST CREST program (1J138), Waseda University Grant for Special Research Projects (2024R-024, 2024C-158).

Declarations

Competing interests
The authors declare no competing interests.

Additional information
Supplementary Information The online version contains supplementary material available at https://doi.org/10.1038/s41598-025-93283-z.

Correspondence and requests for materials should be addressed to K.Y.

Reprints and permissions information is available at www.nature.com/reprints.

Publisher's note Springer Nature remains neutral with regard to jurisdictional claims in published maps and institutional affiliations.

Open Access This article is licensed under a Creative Commons Attribution-NonCommercial-NoDerivatives 4.0 International License, which permits any non-commercial use, sharing, distribution and reproduction in any medium or format, as long as you give appropriate credit to the original author(s) and the source, provide a link to the Creative Commons licence, and indicate if you modified the licensed material. You do not have permission under this licence to share adapted material derived from this article or parts of it. The images or other third party material in this article are included in the article's Creative Commons licence, unless indicated otherwise in a credit line to the material. If material is not included in the article's Creative Commons licence and your intended use is not permitted by statutory regulation or exceeds the permitted use, you will need to obtain permission directly from the copyright holder. To view a copy of this licence, visit http://creativecommons.org/licenses/by-nc-nd/4.0/.

© The Author(s) 2025